










# Effect of structural iron on nanoscroll formation via exfoliation of a high iron-content kaolin

Balázs Zsirka<sup>1,a)</sup>, Katalin Gyórfi<sup>1</sup>, Takahide Yamaguchi<sup>2</sup>, Attila Táborosi<sup>3</sup>,  
Veronika Vágvolgyi<sup>1</sup>, Clara Parameswary<sup>4</sup>, Zoltán Homonnay<sup>4</sup>, Ernő Kuzmann<sup>4</sup>,  
Erzsébet Horváth<sup>1</sup>, János Kristóf<sup>1</sup>

<sup>1</sup>Research Group of Analytical Chemistry/Laboratory for Surfaces and Nanostructures, University of Pannonia, P.O. Box 158, Veszprém 8201, Hungary

<sup>2</sup>Institute of Quantum Beam Science, Graduate School of Science and Engineering, Ibaraki University, 2-1-1, Bunkyo, Mito, Ibaraki 310-8512, Japan

<sup>3</sup>Research Initiative for Supra-Materials, Faculty of Engineering, Shinshu University, 4-17-1, Wakasato, Nagano City, Nagano 380-8853, Japan

<sup>4</sup>Institute of Chemistry, ELTE Eötvös Loránd University, Pázmány Péter s. 1/A, Budapest 1117, Hungary

<sup>a)</sup>Address all correspondence to this author. e-mail: zsirka.balazs@mk.uni-pannon.hu

Zoltan Homonnay was a guest editor of this journal during the review and decision stage. For the JMR policy on review and publication of manuscripts authored by editors, please refer to <http://www.mrs.org/editor-manuscripts>.

Received: 4 July 2022; accepted: 29 September 2022; published online: 20 October 2022

Nanoscroll formation by cascade intercalation–exfoliation method was investigated for a high iron-content kaolin and after the removal of its iron-bearing mineral constituents (goethite, hematite) by 11 M HCl treatment. Hindered kaolinite nanoscroll formation was observed by TEM in both cases, where the 11 M HCl treatment only slightly improved the occurrence of nanoscroll shapes. The presence of minor amounts of well-dispersed, resilient Fe was observed after the exfoliation of 11 M HCl-treated sample, which was identified as structural Fe<sup>3+</sup>/Fe<sup>2+</sup> in the octahedral sheet of kaolinite by Mössbauer and X-ray absorption spectroscopy. Iron substitution in the nanokaolinite TO layers was probed by computational chemistry. The computational results indicate inner coordination changes and elongation of bonds in the iron-substituted TO structure, and the increased curvature values offer an explanation for the observed experimental results for hindered nanoscroll formation.

## Introduction

Kaolinite and its hydrated polymorph, halloysite, are natural, secondary silicate clay minerals, belonging to the group of layered silicates with an empirical formula of Al<sub>2</sub>Si<sub>2</sub>O<sub>5</sub>(OH)<sub>4</sub> (1:1 type dioctahedral phyllosilicates). Numerous interconnected silicon-centered tetrahedral (T-sheet) and alumina-centered octahedral (O-sheet) layers form their double-layered structure with a basal distance of *ca.* 7.2 Å in kaolinite and *ca.* 10 Å in hydrated halloysite. The TO layers have a dipole moment and are joined together by numerous hydrogen bonds between the inner surface hydroxide groups located on the outer surface of the O-sheet, and the bridging oxygens of the T-sheet. Kaolinite displays a characteristic pseudo-hexagonal morphology, while halloysite has a nanoscroll morphology due to the presence of interlayer water molecules [1, 2].

In 1:1 phyllosilicates the TO layers are generally charge-neutral, and while isomorphous substitution of central ions is almost negligible (*e.g.*, Al<sup>3+</sup> to Fe<sup>3+</sup>, Mg<sup>2+</sup>, V<sup>3+</sup>, Ti<sup>4+</sup>, etc.), it can modify the properties of the TO structure, such as inducing permanent, local charges of the surface [3], influencing the surface properties, such as the hydrophobicity and acidity, or causing microstrains in the crystal structure by altering the bond lengths [1, 2, 4].

The abundant, natural, and cheap clay minerals have advantageous and tunable structural and surface properties offering a significant potential in the development and use of clay-based catalysts and adsorbents [5]. The unique nanoscroll morphology and porosity of halloysite is especially promising for catalysis [6]. The presence of active centers and numerous surface hydroxide groups strongly contributes to the adsorption of substrates,

while heterogeneous photocatalysts derived from 1:1 type dioctahedral aluminosilicates [7, 8] offer very promising application in the growing field of environmental technologies as adsorbents and photocatalysts [5]. 1:1 type clay minerals and their surface-modified derivatives could be efficiently used as photocatalysts in the removal of various aqueous and airborne pollutants [9, 10].

Mined kaolin and halloysite may contain various amounts of mineral contaminants (*e.g.*,  $\text{Fe}_2\text{O}_3$ ,  $\text{FeOOH}$ ,  $\text{TiO}_2$ ) that can significantly affect their catalytic activity. The presence of iron containing compounds can contribute to the enhancement of photochemical activity in the degradation of organic pollutants [11] or pesticides [12] and to the synthesis of visible-light harvesting catalysts [13, 14].

The rare isomorphous substitution of Al to Fe in kaolinites could also play an important role in the improvement of intrinsic photocatalytic properties [15]. Iron substitution in clays is considered to follow a random distribution [16], and while  $\text{Fe}^{3+}$  and rarely  $\text{Fe}^{2+}$  can be found in the O-sheet, only  $\text{Fe}^{3+}$  is reported in the T-sheet [17–19].  $\text{Fe}^{3+}$  generally retains the six-fold coordination [20], while  $\text{Fe}^{2+}$  can be present in six- or four-fold coordinations [21, 22] as well. There are a few suitable analytical methods for the investigation of structural iron in clays, Mössbauer spectroscopy [23], X-ray absorption spectroscopy [24], and the slightly less frequently applied X-ray photoelectron spectroscopy [25], being the most often reported.

Acid treatment of high iron-content kaolins can result in the controlled modification of iron impurities and also in yielding kaolins without accompanying iron-bearing mineral contaminants [26]. The presence of  $\text{Fe}^{2+}/\text{Fe}^{3+}$  can be crucial and can catalyze the degradation of some compounds even under ambient conditions [27].

The intrinsic morphology of kaolinite and halloysite can be artificially modified and halloysite-like nanoscrolls with increased surface area and tubular morphology can be synthesized via a multi-step intercalation and exfoliation method [28, 29]. First, a reactive intercalating agent is introduced between the TO layers, resulting in a formation of an organo-complex [30, 31], which can be replaced [32] to weaken the stabilizing hydrogen bonds of the structure. In case of exfoliation, the structural arrangement of crystalline clays disintegrates into individual TO layers, which are consequently rolled up to energetically compensate the changes [33] resulting in the formation of kaolinite nanomaterials having tubular, scrolled morphology [34, 35]. The abundance of these exfoliated nanoscrolls was found to be dependent on the applied synthesis route and the crystallinity of the clays [28].

Kaolinite nanostructures can be applied in various industrial fields, from additives, coatings, and pigments to nanostorage and biomedical applications [36]; however, the recent focus is on their remarkable potential to be photocatalysts [10, 37, 38] or adsorbents [39].

In our previous study [26], the mineral constituents and properties of a high iron-content kaolin was modified by HCl treatment, resulting in a catalytically improved material. Despite the low specific surface area, the surface normalized photocatalytic activity was very promising, indicating the potential of the structure, which could be harnessed at full potential if the specific surface area was increased.

As a continuation of our efforts to develop novel catalysts, the given work provides insight into the exfoliation potential by a cascade intercalation–exfoliation procedure, investigation, and possibility for improvement of the nanoscroll formation of a high iron-content kaolin. The intercalation and exfoliation were followed by X-ray diffraction (XRD) and infrared spectroscopy (FTIR), while the exfoliated nanokaolinite was characterized by transmission electron microscopy (TEM) and energy-dispersive X-ray (TEM–EDX) methods. The presence and effect of structural iron in the kaolinite TO layers were probed by Mössbauer and X-ray absorption spectroscopy (XAS), and computation chemistry was applied for the molecular understanding of nanoscroll formation in Fe-substituted nanokaolinites.

## Results and discussion

### Intercalation and exfoliation of Kao and 11 M-Kao

#### X-ray diffraction

The XRD patterns of the untreated Kao, the 11 M HCl acid-treated Kao and their intercalated samples are shown in Fig. 1. The evaluation of mineral constituents of the pristine Kao sample, and the acid treatment is reported in our antecedent article [26] and is not discussed further here.

The intercalation process can be readily followed by the shift of the kaolinite 001 reflection ( $12.3^\circ 2\theta$ ,  $d(001) = 7.2 \text{ \AA}$ ) to smaller  $2\theta$  values due to the expansion of the interlayer gallery [28]. The intercalation efficiency can be estimated by the integrated intensities of the expanded and non-expanded 001 reflections [40, 41].

After potassium acetate [Fig. 1(b)] intercalation, the observed reflections at  $7.6^\circ$  and  $6.2^\circ 2\theta$  correspond to the hydrated ( $14.1 \text{ \AA}$ ) and dehydrated ( $11.6 \text{ \AA}$ ) potassium acetate present between the expanded kaolinite TO layers [42, 43]. This precursor can be destabilized by heat treatment, and as a result, the intercalation reagent can be exchanged with ethylene glycol [Fig. 1(c)]. The successful replacement with ethylene glycol is indicated by the disappearance of the potassium acetate reflections and the appearance of a new reflection at  $8.1^\circ 2\theta$  belonging to the  $10.9 \text{ \AA}$  basal distance [44, 45]. High intercalation efficiencies (93–98%) were observed for both the untreated and acid-treated kaolinites

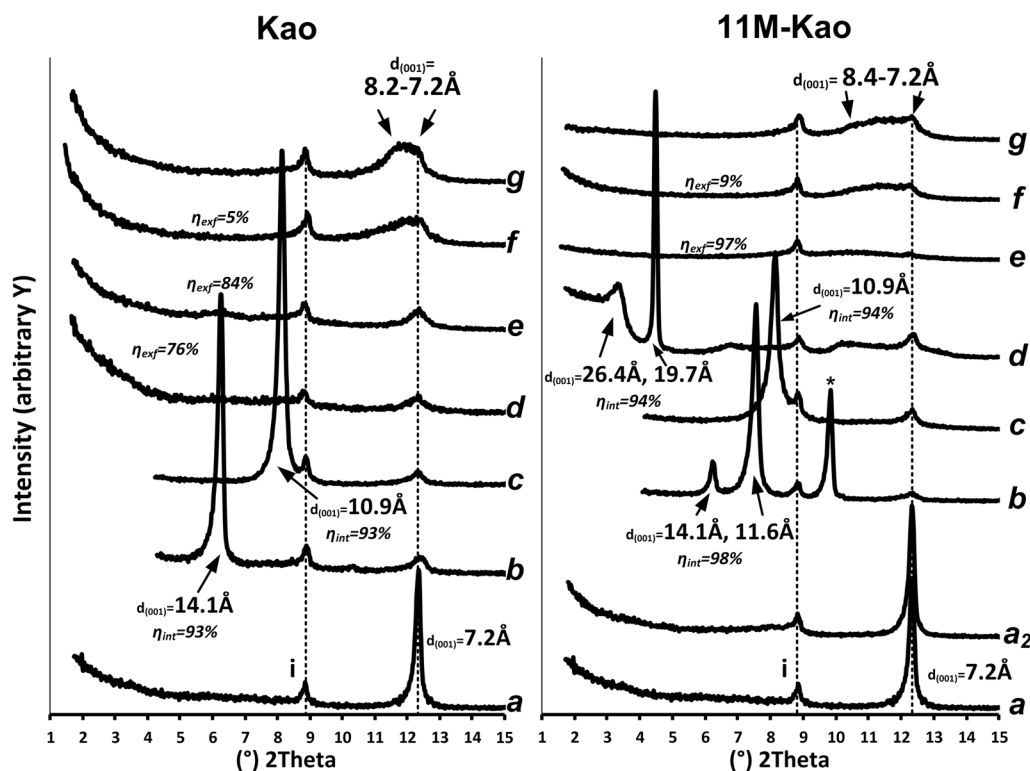


**Figure 1:** XRD patterns following the cascade intercalation of Kao (a) and 11 M-Kao (a2) samples with (b) potassium acetate, (c) ethylene-glycol, (d) hexylamine, (e) toluene, and surface cleaning with (f) 2-propanol, acetone, and water, (g) hydrogen peroxide. The intercalation and exfoliation efficiencies and the 001 interlayer distances of kaolinite are indicated. Note: \* denotes non-intercalated, crystalline potassium acetate reflection, while “i” indicates a reflection belonging to illite phase).

[Fig. 1(b), (c)], indicating that the acid-treated kaolinite can be successfully intercalated. The reflections of hexylamine at  $3.3^\circ$  and  $4.5^\circ$   $2\theta$  belonging to  $26.1 \text{ \AA}$  and  $19.7 \text{ \AA}$  basal distances of the expanded structure [34, 46] are visible in the XRD pattern of the acid-treated sample and are absent in the untreated sample [Fig. 1(d), Kao vs 11 M-Kao]. The absence of these 001 reflections indicates that exfoliation of the expanded kaolinite stacks already took place [28], which can fundamentally be achieved by toluene washing [Fig. 1(d)]. The observed exfoliation efficiency is lower in case of Kao (84%) and is significantly higher in case of 11 M-Kao (97%), indicating that the acid treatment of kaolinite modified its properties (e.g., by possible introduction of surface Al defect sites [26]) and behavior upon disintegration of the crystalline kaolinite phase.

As a result of surface cleaning [Fig. 1(f), (g)], broad, low-intensity reflections appear between *ca.*  $10.1^\circ$  and  $12.3^\circ$   $2\theta$ . These can be assigned to the structural rearrangement of the exfoliated nanoparticles [Fig. 1(f)] due to the hydrogen bonding interactions of the exposed surface hydroxide groups [29, 35]. The phenomenon is more prominent after oxidative surface treatment [Fig. 1(g)], revealing variously hydrated, agglomerated kaolinite

nanoparticles having basal distances of *ca.*  $8.4\text{--}7.2 \text{ \AA}$  [47, 48]. The degree of this reconstitution is slightly less prominent for the 11 M-Kao sample, which might be due to the marginally different morphology of the kaolinite nanoparticles [Fig. 3/nKao vs 11 M-nKao]; however, this difference vanishes after oxidative surface cleaning, and afterward, no exfoliated particles can be identified in the XRD patterns.

The kaolinite crystallite thickness along the *c*-axis and the number of adjoined TO layers can also be estimated by the 001 reflection using the Scherrer equation [49]. The calculated values are summarized in Table S1. Pristine kaolinite showed to have in average 480 interconnected TO layers in a crystallite, which changed insignificantly after acid treatment (Table S1/Kao vs 11 M-Kao). The average crystallite size of the rearranged nanokaolinites is difficult to estimate, due to the presence of overlapping bands belonging to slightly differently hydrated particles (Figure S1/nKao, 11 M-nKao). However, given that the FWHM values of the oxidatively treated nKao (*ca.*  $1.80^\circ$ ) and 11 M-nKao (*ca.*  $1.18^\circ$ ) are significantly broader than the pristine Kao and 11 M-Kao (*ca.*  $0.18^\circ$ ), it is evident that the average crystallite size and, consequently, the average number of TO layers are decreased significantly.

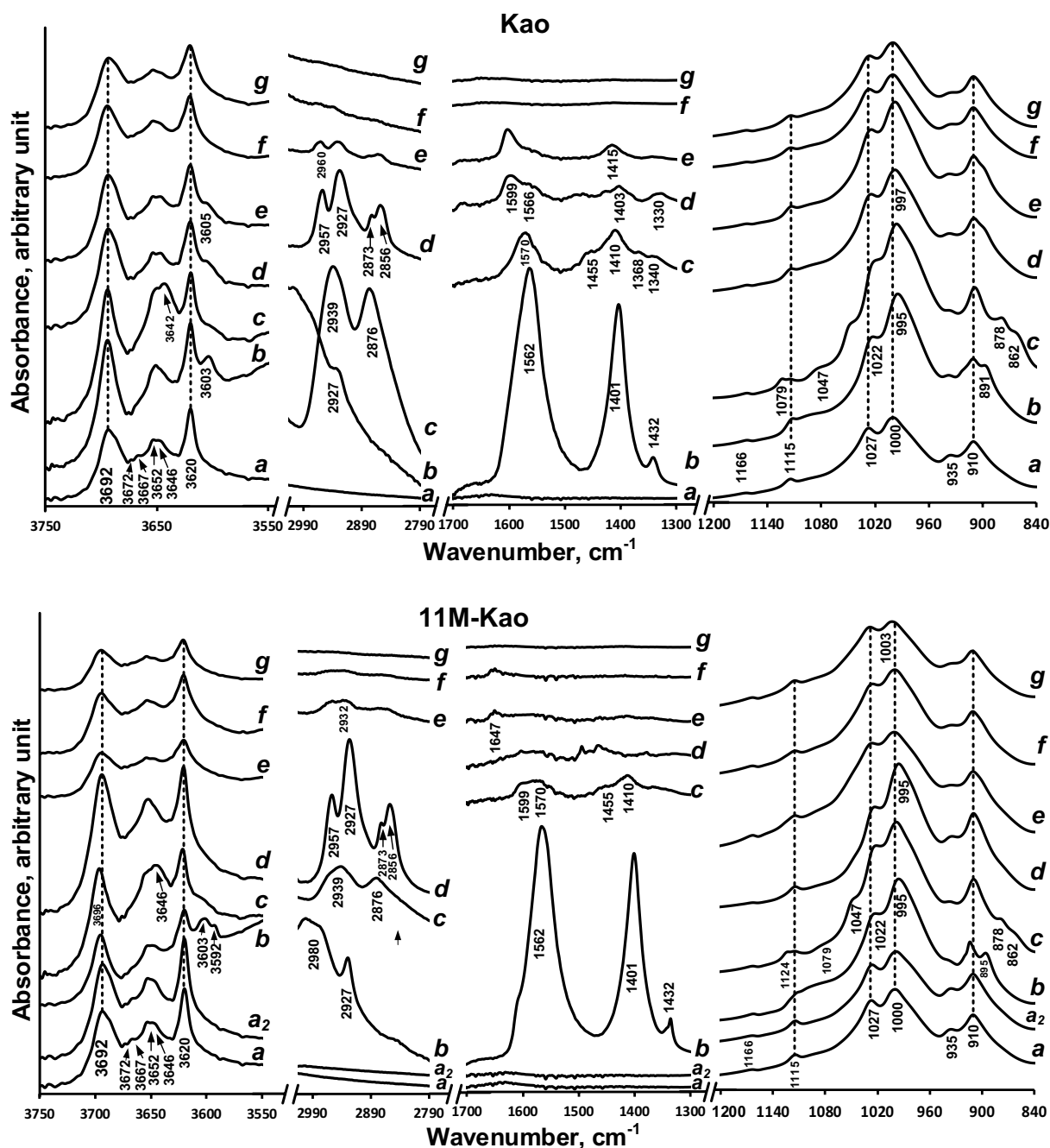


**Figure 2:** FTIR-ATR spectra of Kao (a) and 11 M-Kao (a<sub>2</sub>) samples, intercalated with b potassium acetate, c ethylene glycol, d hexylamine, e toluene, and after surface cleaning with f 2-propanol, acetone, and water, g hydrogen peroxide, displayed in the spectral regions of interest. Note: “g” and “f” spectra in the 2790–3015 cm<sup>-1</sup> region are displayed with 2× magnification.

### FTIR spectroscopy

The FTIR-ATR spectra of the untreated Kao, the 11 M-Kao, and their intercalated derivatives in the spectral regions of interest are shown in Fig. 2, while the whole spectra are given in Figure S2.

The untreated Kao sample displays the characteristic vibrational features of kaolinite, based on the observed group

frequencies belonging to the (Al)-OH groups of the O-sheet (Fig. 2/3620–3695 cm<sup>-1</sup>, 910–940 cm<sup>-1</sup>) and Si-O groups of the T-sheet (1000–1115 cm<sup>-1</sup>, 800–740 cm<sup>-1</sup>) [50, 51]. The νOH region of kaolinite is quite unique, having 4 bands at 3692, 3667, 3652 cm<sup>-1</sup> (assigned to inner surface hydroxides), and 3620 cm<sup>-1</sup> (assigned to inner hydroxides) [52]. The distinctive bands at ca. 3600 cm<sup>-1</sup> (ν(Fe-Al)-OH) and ca. 880 cm<sup>-1</sup>



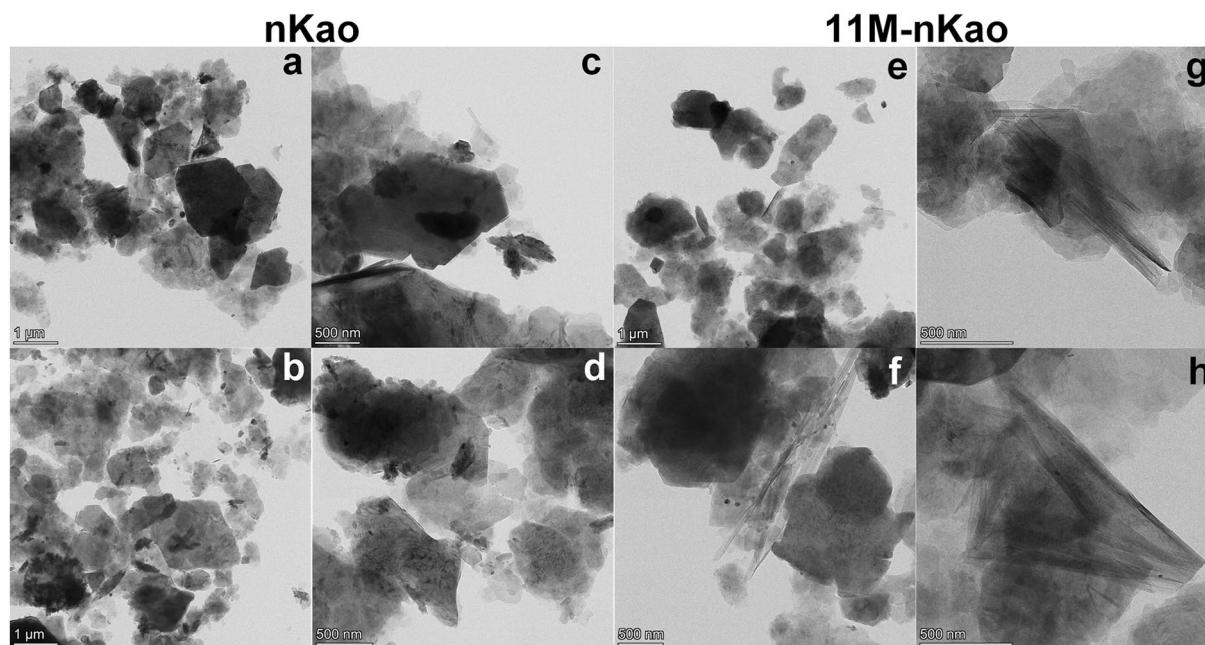


**Figure 3:** Typical TEM images of exfoliated nKao (a-d) and 11 M-nKao (e-h) samples.

( $\delta(\text{Fe-Al})\text{-OH}$ ) usually observed in Fe-substituted kaolinites [53, 54] are absent [Fig. 2(a)]; however, the two low-intensity bands at  $3672$  and  $3646\text{ cm}^{-1}$  might be indicative of a modified octahedral environment near the (Al)-OH groups, possibly due to structural defect sites as a result of Fe substitution. No significant alterations can be observed in the 11 M-Kao spectra [Fig. 2(a2)], indicating the negligible effect of HCl treatment on the kaolinite structure.

The intercalation process can be verified and followed by the bands of intercalation agents in the organocomplexes (Fig. 2(b-d),  $2800\text{--}3000\text{ cm}^{-1}$ ,  $1300\text{--}1700\text{ cm}^{-1}$ ) and the changes of kaolinite structural vibrations (Fig. 2(b-d),  $3620\text{--}3695\text{ cm}^{-1}$ ,  $1000\text{--}1115\text{ cm}^{-1}$ ,  $910\text{--}940\text{ cm}^{-1}$ ) [55, 56]. The successful intercalation of potassium acetate is indicated by the appearance of  $\nu\text{COO}^-$  ( $1562$ ,  $1401\text{ cm}^{-1}$ ),  $\nu\text{CH}/\delta\text{CH}$  ( $2927$ ,  $1432\text{ cm}^{-1}$ ) vibrations and the  $3603\text{ cm}^{-1}$  band, latter which is assigned to the acetate ion hydrogen-bonded to the inner surface hydroxide groups of kaolinite [57, 58]. Similarly, the intercalation of ethylene glycol and hexylamine is indicated by the presence of the  $\nu\text{OH}$  ( $3300\text{ cm}^{-1}$ ), the symmetrical  $\nu\text{NH}/\delta\text{NH}$  ( $3317$ ,  $1599\text{ cm}^{-1}$ ), and  $\nu\text{CH}/\delta\text{CH}$  ( $2856\text{--}2690\text{ cm}^{-1}$ ,  $1330\text{--}1432\text{ cm}^{-1}$ ) bands [34, 45]. The absent asymmetrical  $\nu\text{NH}$  band is indicative of the intercalated hexylamine [Fig. 2(d)]. The structural alterations resulting from the intercalation are also visible in the Al-OH stretching ( $3600\text{--}3695\text{ cm}^{-1}$ ) and deformation region ( $910\text{--}940\text{ cm}^{-1}$ ) as shifts and new bands appear [Fig. 2(b-d)].

Only subtle changes can be observed after the exfoliation of kaolinite in the structural vibrations regions [52], such as the

slight broadening of  $\nu\text{Si-O}$  vibrations and of the inner surface hydroxide [Fig. 2(e-g)].

The efficiency of surface treatment can be verified by the disappearance of  $\nu\text{CH}_2/\nu\text{CH}_3$  bands [Fig. 2(f-g)], as the majority of the intercalation reagents can be removed by washing (2-propanol, acetone, MilliQ water); however, the strongly bound compounds can only be completely removed upon oxidative surface treatment by  $\text{H}_2\text{O}_2$  [29].

### Evaluation of the nanoscroll formation via the exfoliation process

#### Transmission electron microscopy

The TEM images of the nanokaolinite samples exfoliated from Kao and 11 M-Kao are shown in Fig. 3. The morphological features of the untreated Kao and its acid-treated derivatives are published in our previous study [26].

Despite the exfoliation, the expected tubular, scroll-like morphology of exfoliated kaolinite nanoscrolls are seldom visible [35, 59], and mostly the typical, flat pseudo-hexagonal morphology of kaolinite can be identified in the TEM images, along with agglomerated particles (Fig. 3(a-d)), similarly to the reports of synthetic kaolinites having high structural Fe/Al substitution [53]. However, as a result of exfoliation, small, thin particles are observed, indicating that the average number of adjoined TO layers is decreased (Fig. 3(b,d), Table S1). Since it was present in the original kaolin [26], some co-mineral

impurities, such as goethite, hematite, or anatase, are expected even after the cascade intercalation of Kao.

As a result of 11 M HCl treatment, hematite and goethite mineral phases are removed (Fig. 7, Mössbauer) and Al defect sites could be introduced on the surface [26]. No major differences are observed in the dominant morphology of 11 M-nKao compared to nKao, as flat, pseudo-hexagonal structures are most frequently found in the TEM images (Fig. 3(e,f)). However, the incidence of tubular nanoscrolls slightly increased, with the occurrences of multiple bundled or even partially rolled-up nanoscrolls (Fig. 3(g, h)). These observations indicate that the nanoscroll formation is hindered, even after HCl treatment of the pristine Kao sample.

The presence and distribution of Fe was probed by STEM-EDX, the resulting distribution maps are presented in Fig. 4, and the determined elemental compositions of the investigated areas are summarized in Table S2. It is evident that iron-bearing minerals are present in the nKao sample (Fig. 4/Fe), while only uniformly distributed, minor amounts of Fe are observed in the 11 M-nKao sample. This would indicate the presence of a very stable, resilient iron in minor quantities (*ca.*  $0.7 \pm 0.1$  m/m%, Table S2), most probably incorporated in the TO layers, as it is detected afterward acid treatment and the numerous steps and washing stages of the subsequent intercalation–exfoliation procedure.

### Mössbauer spectroscopy

The Mössbauer spectrum of the pristine kaolin sample Kao (Fig. 5) at room temperature could be evaluated including the following components: a well-resolved sextet assigned to hematite with isomer shift of 0.38 mm/s, magnetic hyperfine field (induction) of  $B = 49.4$  T and quadrupole shift value of  $-0.22$  mm/s; a rather partially collapsed (magnetic relaxation distorted) second sextet with isomer shift of 0.35 mm/s, magnetic hyperfine field of  $B = 29.4$  T and quadrupole shift value of  $-0.27$  mm/s; two paramagnetic doublets, an  $\text{Fe}^{3+}$  with isomer shift value of 0.34 mm/s and quadrupole splitting of 0.59 mm/s and an  $\text{Fe}^{2+}$  with isomer shift of 1.35 mm/s and quadrupole splitting of 2.31 mm/s. The parameters of the doublets were measured later more accurately after rigorous (11 M) HCl treatment. Details of the evaluated parameters are given in Table S3.

The assignment of hematite is quite clear as the hyperfine parameters match literature values [60]. On the other hand, goethite shows up normally with a magnetic hyperfine field about  $B = 38.0$  T at room temperature and quadrupole shift  $-0.26$  mm/s. In our case, the partially collapsed magnetic splitting ( $B = 29.4$  T only) may be attributed to defect structure or low particle size. Both can weaken the long-range interaction responsible for antiferromagnetic coupling, resulting in lower magnetic hyperfine field, but they do not affect much of the local hyperfine parameters as the isomer shift and the quadrupole shift.

Magnetic relaxation can be damped by lowering the temperature. In addition to the two paramagnetic doublets, the 80 K Mössbauer spectrum of Kao shows two sextets with parameters very close those of regular (bulk) hematite and goethite (Fig. 5). However, the two sextets are highly overlapped that hinders the correct evaluations. It may be noted that in general, relaxation phenomena make spectrum evaluations more difficult, but in our case, at room temperature, the relaxation distorted spectrum of goethite and the normal spectrum of hematite can be much better separated. The relaxation distortion of the spectrum of goethite was handled in the evaluations by allowing different line widths for the 1–6, 2–5, and 3–4 couples of the sextet lines, and allowing a relative intensity for the 2–5 couple different from the 3:2:1:1:2:3 ratio.

Hematite exhibits special characters: it is weakly ferromagnetic between the Curie temperature ( $T_C$ ) and Morin temperatures ( $T_M$ ), and antiferromagnetic below  $T_M$ . For pure, well-crystallized hematite, the  $T_C$  and  $T_M$  are about 264 K and 955 K, respectively [61]. The quadrupole shift is characteristic for each magnetic type: it is around  $-0.20$  mm/s for weakly ferromagnetic hematite, and 0.41 mm/s for antiferromagnetic hematite [60].

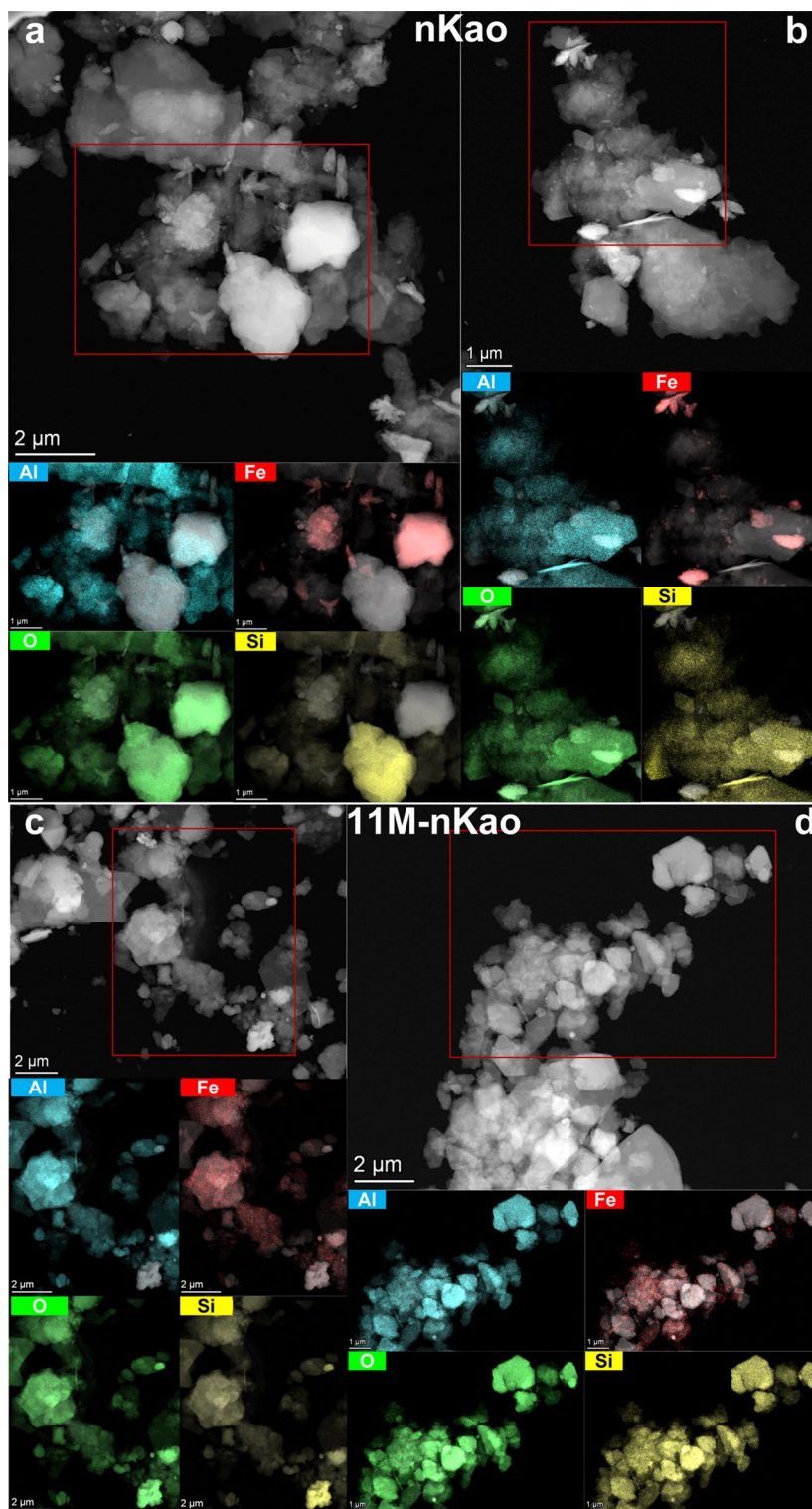
The Morin temperature in our case was absent (the quadrupole shift remained negative at 80 K) which can logically be assigned to Al substitution in hematite as known from literature reports [62]. The slightly lower hyperfine magnetic field compared to that of bulk hematite can also be assigned to the Al impurity.

One may notice that the relative intensities of goethite and hematite are different in the Mössbauer spectra recorded at 80 K and at room temperature. This can be attributed to the different temperature variations of the Mössbauer-Lamb factors for the two phases (different Debye temperatures). The 80 K data are more reliable where the Mössbauer-Lamb factors are not expected to differ substantially.

The presence of hematite and goethite in the Kao sample was also verified by XRD, which phases can be removed upon acid treatment (as was reported earlier in our previous work [26]).

The Mössbauer spectra of acid-treated samples with an HCl concentration up to 8 M clearly show that hematite was dissolved (the well-resolved sextet disappeared from the spectra), but goethite remained (Fig. 6(a–c)). One might be surprised that an oxyhydroxide resists the attack of HCl more than an oxide but, beyond some kinetical reasons [63], it was found by Schwertmann [64] that the solubility and dissolution rate of highly aluminum-substituted iron oxides/oxyhydroxides (especially goethite, since aluminum substitution occurs with higher probability in this mineral) in HCl solution are considerably decreased. These evidences hence justify the proposed assignment of the relaxed component

**Figure 4:** STEM images and corresponding Al (cyan blue), Fe (red), O (green), Si (yellow) distribution maps from the highlighted areas of exfoliated nKao (a, b) and 11 M-nKao (c, d) samples by STEM-EDX measurements.



observed in the Mössbauer spectra to aluminum-substituted goethite.

In the Mössbauer spectra of samples, containing the sextets of goethite or goethite + hematite, the evaluation of the

paramagnetic  $Fe^{2+}$  and  $Fe^{3+}$  components is very uncertain due to the strong overlap with the sextets.

Nevertheless, when Kao was treated with 11 M HCl, the removal of goethite was also complete, only the quadrupole



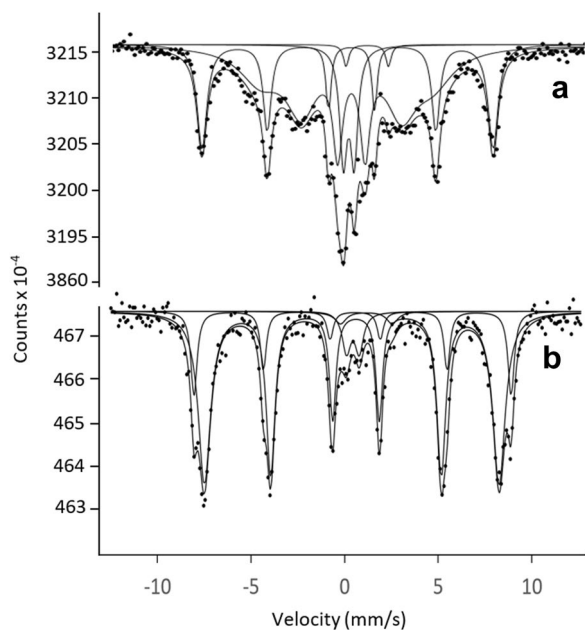


**Figure 5:** Mössbauer spectrum of the Kao sample recorded at room temperature (a) and at 80 K (b).

doublets showed up in the spectra. The Mössbauer spectrum of the 11 M HCl-treated sample (Fig. 6(d)) was recorded in narrower velocity range for better resolution and for more accurate hyperfine parameters.

These paramagnetic components are logically assigned to  $\text{Fe}^{2+}$  and  $\text{Fe}^{3+}$  located in the TO layers, most probably due to the isomorphous substitution of Fe for Al in the octahedral layer. There are literature reports of  $\text{Fe}^{3+}$  as structural iron,

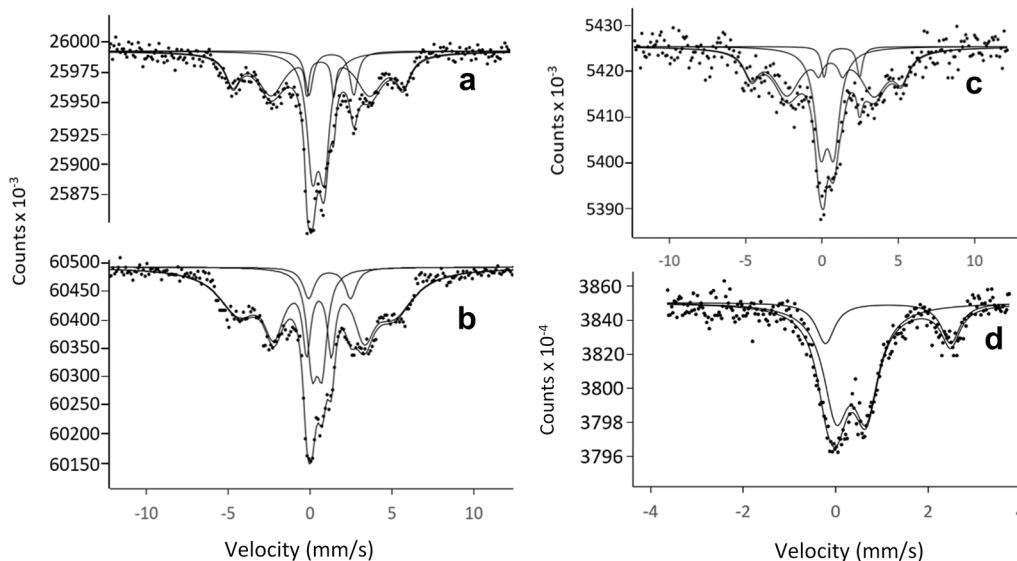


**Figure 6:** Room-temperature Mössbauer spectra of sample Kao treated with 8 M HCl for 3 h (a), with 5 M HCl for 6 h (b), with 5 M HCl for 6 h + 0.1 M HCl solution for 24 h (c), and with 11 M HCl for 6 h (d), the latter recorded in narrower velocity range for higher resolution.

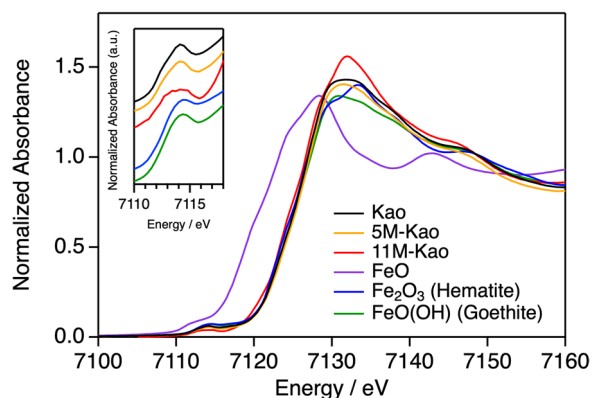


**Figure 7:** The XANES region of Fe K-edge X-ray absorption spectra of Kao (black), 5 M-Kao (orange), 11 M-Kao (red) samples compared to FeO (purple), hematite (blue), and goethite (green). Inset: pre-edge region (7110–7118 eV).

and also  $\text{Fe}^{2+}$  which can be present to compensate for the higher ionic charge of other substituents in the octahedral layer (e.g.,  $\text{Ti}^{4+}$ ,  $\text{Si}^{4+}$ ) [65].

Although 1:1 phyllosilicates can contain structural  $\text{Fe}^{2+}$  or  $\text{Fe}^{3+}$  in the O-sheet and  $\text{Fe}^{3+}$  in the T-sheets [17], the Mössbauer isomer shifts clearly show only octahedrally coordinated structural iron in the Kao and its acid-treated samples. The Mössbauer parameters of the doublets could be measured accurately in this case: isomer shifts 0.34(1) mm/s and 1.14(2) mm/s, quadrupole splitting 0.65(2) mm/s and 2.71(4) mm/s for  $\text{Fe}^{3+}$  and for  $\text{Fe}^{2+}$ , respectively, at room temperature. Both  $\text{Fe}^{3+}$  and  $\text{Fe}^{2+}$  are unquestionably in high spin state.



The Mössbauer parameters of the observed doublets may allow an assignment to Fe substituted for Al in illite [66], a minor mineral impurity in our Kao sample, but illite is present only in a small volume fraction, and STEM-EDX measurements verified an even distribution of iron in nKao and 11 M-nKao microcrystals. Thus, the possible contribution of the illite minor phase to the Mössbauer spectra is neglected.

To verify the presence of structural iron, its coordination environment was examined by EXAFS, as recommended by literature [17], and the six-fold coordination by oxygens was confirmed.

### X-ray absorption spectroscopy

#### Fe K-edge XANES of Kao, 5 M-Kao, 11 M-Kao, and iron oxides

Figure 7 shows the XANES of Fe K-edge spectra of Kao, its 5 M and 11 M HCl (6 h)-treated derivatives, and references. The rising edge position of the untreated Kao sample was around 7123.0 eV. The rising edge energy is identical with that of Fe<sub>2</sub>O<sub>3</sub> (hematite) and FeO(OH) (goethite) and clearly different than that of FeO. Thus, the average Fe oxidation state of untreated Kao sample is trivalent. The untreated Kao sample also shows broadened peak with the center energy of 7132.0 eV at the top of XANES. The Fe composition of Kao determined by Mössbauer spectroscopy is 18.2 ± 2.6% hematite and 73.8 ± 3.6% goethite as the major components (Table S3/80 K). The composition analyses were also performed by simulating XANES of Kao in Figure S3. The spectral features of simulated XANES by 20–30% hematite and 70–80% goethite in Figure S3(B, C) are similar to Kao, which confirms the composition analysis of Kao sample by Mössbauer spectroscopy (Fig. 5).

The composition analysis of Mössbauer spectroscopy also demonstrated the removal of hematite by 5 M HCl treatment (Fig. 6). The peak in the XANES of 5 M-Kao was slightly shifted to 7131.2 eV (Fig. 7, -0.8 eV from Kao), which is observed closer to the goethite peak (7130.8 eV), indicating that goethite is present after 5 M HCl treatment.

The XANES of the 11 M HCl-treated Kao sample was clearly different from the untreated and 5 M HCl-treated samples. The peak energy of 11 M-Kao sample was 7132.0 eV. The rising edge energy of 11 M-Kao was essentially the same as for hematite and goethite, but the subtle contribution of lower energy edge could be recognized in the first-derivative spectra (Figure S4). These observations indicate that: (1) the oxidation state of Fe incorporated in kaolinite octahedral site as structural Fe is dominantly trivalent, and (2) the possibility of divalent Fe is expected as a minor constituent.

#### Fe K-edge EXAFS of Kao, 5 M-Kao, 11 M-Kao, and iron oxides

EXAFS of the clays and iron oxides are shown in Fig. 8 in *R*-space, Figure S5 in *k*-space. Note the “distance” in Fig. 8 bottom axis cannot be correlated directly to the actual distance due

to the phase shift contribution. EXAFS of all samples shows the peak (i) approximately at 1.5 Å in the first shell region of *R*-space. These peaks were assigned as the Fe–O distance because the Fe is directly coordinated by O in all cases of hematite, goethite, and structural Fe. In the outer sphere, additional peaks, marked as (ii) and (iii), appeared in the hematite, goethite, untreated Kao, and 5 M acid-treated Kao (ca. 2.5 Å and 3.1 Å, respectively, in *R*-space), which were assigned as Fe–Fe contributions (fitting analysis in the following paragraph). The amplitude of these peaks was decreased by 5 M HCl treatment compared to the untreated Kao; furthermore, these peaks were absent from the 11 M HCl-treated kaolin. This is a very clear evidence that the hematite and goethite were removed by the 11 M acid treatment and supports the Mössbauer results (Fig. 6(d)) and our previously reported observations [26].

Figure S6 shows the fitting of EXAFS of hematite, goethite, and 11 M HCl-treated Kao, and the analyzed Fe-surrounding distances are summarized in Table 1. The EXAFS data of untreated Kao and 5 M-Kao were excluded from the fitting analysis because the EXAFS analyses of these kaolins cannot provide the accurate structural information as the samples were mixtures of iron oxides and kaolinite with structural iron. The fitting on the EXAFS of hematite (Figure S6/A) indicated the first shell peak of hematite stems from Fe–O scattering pathway with the distance of 1.98 ± 0.01 Å, and 3 Fe–Fe scattering pathways (2.93 ± 0.01 Å, 3.36 ± 0.01 Å, 3.65 ± 0.01 Å) contribute in outer shell. In a similar manner, the first shell of goethite could be fitted by 2.00 ± 0.01 Å Fe–O pathway, and the contribution of 3 Fe–Fe scattering pathways (2.97 ± 0.06 Å, 3.11 ± 0.07 Å, 3.36 ± 0.03 Å) exists in outer shell (Fig. S6(B)). From both the hematite and goethite EXAFS data, we assign the outer shell EXAFS peaks to Fe–Fe distances. The first shell peak of 11 M HCl-treated Kao was determined to be 2.04 ± 0.01 Å from the fitting in Fig. S6(C). The Fe–O distance at the structural Fe site slightly elongated by 0.04–0.07 Å relative to hematite and goethite. Although the inclusion of Fe–Al peak at 3.15 ± 0.07 Å

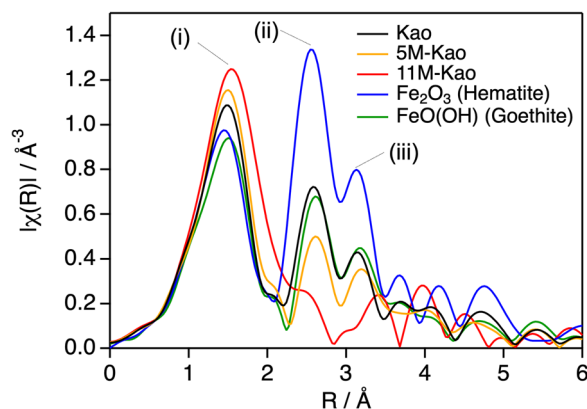


**Figure 8:** Fe K-edge EXAFS of untreated Kao (black), 5 M HCl-treated (orange), and 11 M HCl-treated (red) Kao compared to hematite (blue) and goethite (green) in *R*-space.

and Fe–O peak at  $3.85 \pm 0.04 \text{ \AA}$  was necessary for the fitting of outer shell, the Fe–Fe contribution cannot be found in the 11 M-Kao sample. The missing of Fe–Fe EXAFS peak indicates that the structural Fe is dispersedly doped, which is consistent with STEM-EDX results (Fig. 4) and the random occurrence of structural Fe substitution [16].

### Computational chemistry

Computational chemistry was utilized to probe the molecular structure of kaolinite with structural iron. The computational study of Richard et al. showed that the utilization of GIPAW-D2 + U method could describe the electronic structure of Al substituted for Fe atom and together with the Mössbauer data, it had been found that the both  $\text{Fe}^{3+}$  and  $\text{Fe}^{2+}$  can exist in the kaolinite layers, but only in high spin state form [19].

Three positions of  $\text{Al}^{3+}$  in the central honeycomb were considered to be replaced with  $\text{Fe}^{3+}/\text{Fe}^{2+}$  cations to determine the structural changes in the central honeycomb of nanokaolinite. Besides the expected high spin, the low spin state of Fe was also considered in the computations. The symmetry axis of the central honeycomb (Figure S7) allowed us to consider only three positions in the central honeycomb instead of all six positions. The inter/intramolecular distances listed in Table S4 were chosen to compare the structural differences before and after the replacement of  $\text{Al}^{3+}$  and to investigate the existence of structural  $\text{Fe}^{3+}/\text{Fe}^{2+}$  proposed by the Mössbauer and XAS studies (chapters 3.2.2. and 3.2.3.).

The calculated energies of each positions (Figure S7/ P1, P2, P3) in both high and low spin states for each oxidation state were compared (Table S5). The energy difference between the positions is neglectable (around 10 kJ/mol), indicating that all three positions are viable for the Fe to exist in the structure of kaolinite, which is in agreement with the reported random distribution nature of structural iron [16]. However, the Boltzmann distribution values might indicate the preference of P1 and P2 substitution in the structure.

The energy difference between  $\text{Fe}^{2+}$  spin states is significant ( $\sim 60\text{--}70 \text{ kJ/mol}$ ), indicating a preferable possibility of only the high spin state. While the energy difference of low and high spin state of  $\text{Fe}^{3+}$  is quite small ( $\sim 7 \text{ kJ/mol}$ ), the calculated Boltzmann distribution indicate the almost exclusive presence of high spin states for both  $\text{Fe}^{2+}$  and  $\text{Fe}^{3+}$ , which is in agreement with the literature [4, 19].

Comparing the computed Fe–O distances with EXAFS fitting results (Table 1) shows that high spin  $\text{Fe}^{3+}$  Fe–O distances are similar (Fe–O =  $2.04 \text{ \AA}$ ), suggesting that structural  $\text{Fe}^{3+}$  in high spin state is the most likely to exist.  $\text{Fe}^{2+}$  low spin Fe–O distances (Table S4) gave also similar distances ( $\sim 2.04 \text{ \AA}$ ); however, the energetic comparison (Table S5) ruled out the possibility of  $\text{Fe}^{2+}$  low spin structural existence. Therefore, only the high spin states of Fe are discussed further.

The Al–O ( $\text{sOH}^-$ ,  $\text{iHO}^-$ ,  $\text{aO}^{2-}$ ), Al–Al, and Al–Si distances are identical on all three chosen positions (Table S4). The same trend can be seen for  $\text{Fe}^{3+}$  or  $\text{Fe}^{2+}$ , indicating that the position of Fe replacement does not affect the distances. However, different inner coordinates can be observed depending on the Fe oxidation states. The  $\text{Fe}^{3+}$  shows already great elongation on both Fe–O bonds and Fe–Al/Fe–Si distances compared to  $\text{Al}^{3+}$  inner coordinates. Thus, the Fe–O bonds increased by  $\sim 0.13 \text{ \AA}$  and Fe–Al/Fe–Si distances elongated by  $\sim 0.1 \text{ \AA}$ . The  $\text{Fe}^{2+}$  configuration even shows greater expansion of Fe–O bonds compared to  $\text{Fe}^{3+}$ , with the increase of  $\sim 0.22 \text{ \AA}$ , but the Fe–Al/Fe–Si distances are the same as for  $\text{Fe}^{3+}$ .

It was experimentally observed that the nanoscroll formation is hindered after exfoliation of kaolinite, with only a slight increase even after the removal of iron-bearing co-minerals by 11 M HCl treatment (Fig. 3). Li and coworkers determined with theoretical calculation that the minimum interior diameter for a single kaolinite sheet to be scrolled is about  $9.08 \text{ nm}$  ( $R = 45.4 \text{ \AA}$ ), the optimal is  $24.30 \text{ nm}$  ( $R = 121.5 \text{ \AA}$ ), and the maximum is  $100 \text{ nm}$  ( $R = 500 \text{ \AA}$ ) [67]. In our previous study [52], the optimal curvature for an optimal, defect-free nanokaolinite ( $G_2$  model, PW91 + D/SVP/PCM) was determined to be around  $67.6 \text{ \AA}$  ( $13.52 \text{ nm}$ ), which is less than the experimentally observed optimal curvature of  $121.5 \text{ \AA}$  (Table 2) [35, 59]. The calculated minimal curvature value for the  $G_2$  models is  $22.7 \text{ \AA}$ , with the optimum of  $67.6 \text{ \AA}$  and maximum of  $200 \text{ \AA}$ . The formation of nanoscrolls is less probable as getting closer to the maximum value, and if the curvature value exceeds the maximum value, the formation of nanoscrolls is generally inhibited. Table 2 summarizes all the calculated values for  $G_2\text{-Al}$ ,  $G_2\text{-Fe}^{3+}$ , and  $G_2\text{-Fe}^{2+}$  models in high spin states. In all cases, Al replacement with Fe increased the curvature value by  $\sim 170\text{--}217 \text{ \AA}$ , regardless of oxidation state, which has an effect also on the scrolling of nanokaolinite. The Fe–O distances increased as compared to the Al–O distances (Table S4) also impacting the curvature. Both oxidation states of Fe high spin states showed increase in

**TABLE 1:** Fe surrounding distances determined by the EXAFS fitting.

Sample	Scattering pathway		
	Fe–O	Fe–Fe	Fe–Al
	distance/ $\text{\AA}$ (degeneracy)		
Hematite	$1.98 \pm 0.01$ (6)	$2.93 \pm 0.01$ (3)	
		$3.36 \pm 0.01$ (3)	
		$3.65 \pm 0.01$ (6)	
Goethite	$2.00 \pm 0.01$ (6)	$2.97 \pm 0.06$ (2)	
		$3.11 \pm 0.07$ (2)	
		$3.36 \pm 0.03$ (4)	
11 M-Kao	$2.04 \pm 0.01$ (6)		$3.15 \pm 0.07$ (3)
	$3.85 \pm 0.04$ (6)		

the inner coordinates, especially for  $\text{Fe}^{2+}$  high spin. This resulted in the simultaneous increment of the  $R$  curvature values as well, which exceeded the maximum limit of possible formation of nanoscrolls ( $> 200 \text{ \AA}$ ). Computational results indicate that the most preferable Al replacement is the  $\text{Fe}^{3+}$  high spin state, where the too high  $R$  curvature value ( $R = 238 \text{ \AA}$ ) explains the observed hinderance of nanoscroll formation when  $\text{Fe}^{3+}$  exists in the O-sheet.

## Conclusion

Hindered nanoscroll formation and rearranged kaolinite nanoparticles were observed after a partial exfoliation of a high iron-content kaolin (Kao), which is only slightly improved after the removal of iron-bearing mineral constituents by 11 M HCl treatment (11 M-Kao). The dominant morphology was found to be mostly uncurled pseudo-hexagonal, with only minor occurrences of nanoscrolls in both cases. STEM-EDX atomic distribution images revealed the presence of a minor amount of Fe in the exfoliated 11 M HCl-treated sample, even after intercalation–exfoliation–washing cycles, indicating its resilience.

The hinderance in the roll-up of exfoliated kaolinite nanosheets was hypothesized to be due to the presence of structural Fe as a result of isomorphous substitution in the TO layers. Mössbauer spectroscopy results confirmed the presence of structural  $\text{Fe}^{3+}/\text{Fe}^{2+}$  in the octahedral sheet of kaolinite, which was still detected even after 11 M HCl acid treatment. X-ray absorption spectroscopy confirmed the presence of a well-dispersed structural iron ( $\text{Fe}^{3+}/\text{Fe}^{2+}$ ) in the 11 M-Kao sample. The Fe substitution in the octahedral sheet was investigated by computational chemistry, indicating that nanoscroll formation is hindered most probably due to the elongated Fe–O distances and the inner coordination changes when high spin  $\text{Fe}^{3+}$  or  $\text{Fe}^{2+}$  is incorporated in the O-sheet. The results explain the experimental observations of the low nanoscroll occurrence rate and indicate that the nanoscroll exfoliation is disadvantageous when structural iron is present in the TO layers. The presence of structural  $\text{Fe}^{3+}$  and  $\text{Fe}^{2+}$  in the kaolinite TO layers could contribute

to their enhanced photocatalytic activity and the possibility of the formation of a light-sensitive, photoactive complex during oxalic acid irradiation, as reported in our previous studies [26, 68]. The results should be taken into consideration for future natural, kaolinite-based catalysts development designs.

## Materials and methods

### Materials

The natural, high iron-content kaolin (Kao) studied is from Felsőpetény, Hungary. The kaolin sample dominantly consists of kaolinite, with some goethite, hematite, quartz, illite, and anatase as co-minerals [26]. The oxidic composition of the sample designated as **Kao** is as follows: 56%  $\text{SiO}_2$ , 22%  $\text{Al}_2\text{O}_3$ , 5.6%  $\text{Fe}_2\text{O}_3$ , 1.0%  $\text{TiO}_2$ , 0.3%  $\text{CaO}$ , 0.6%  $\text{MgO}$ , 1.1%  $\text{K}_2\text{O}$ , and 0.1%  $\text{Na}_2\text{O}$  (m/m%). Samples having particles sizes smaller than  $125 \mu\text{m}$  were used in the study.

The applied chemicals were as follows: potassium acetate ( $> 99\%$ , VWR International), ethylene glycol (99.8%, anhydrous, Sigma-Aldrich), *n*-hexylamine (99%, Sigma-Aldrich), toluene ( $> 99\%$ , Scharlau), 2-propanol (99%, Sigma-Aldrich), acetone ( $> 99\%$ , Sigma-Aldrich), hydrochloric acid (37%, VWR International), and MilliQ water (conductivity  $< 0.056 \mu\text{S}/\text{cm}$ ).

### Acid treatment

The effect of hydrochloric acid treatment on the mineral composition and properties of the studied Kao has been reported in our previous study [26]. Based on these results, the acid treatment of 5 M, 8 M, and 11 M  $\text{HCl}_{(\text{aq})}$  was applied to modify the samples: ca. 2 g Kao was mixed with 10 mL of the corresponding acids and vigorously stirred for 3–6 h. After acid treatment, the samples were rinsed with MilliQ water and centrifuge separated (5000 rpm, 5 min). This washing process was repeated 4 times to remove surface-adsorbed HCl, then the samples were dried at room temperature and ground.

The designation of the acid-treated samples is as follows: YM-Kao, where Y is the molarity of the applied HCl.

**TABLE 2:** The experimental structural parameters without ( $G_2\text{-Al}$  [52]) and with Fe presence ( $G_2\text{-Fe}^{3+}$ ,  $G_2\text{-Fe}^{2+}$ ) in Al honeycomb to determine the curvature ( $R$ ,  $\text{\AA}$ ) of the tubular, scroll-like nanokaolinite, where  $d(\text{O})$  and

$d(\text{T})$  represent the diameters of the Al and Si honeycombs and  $h$  stands for the thickness of the TO sheet [67].

			$d(\text{T}), \text{\AA}$	$d(\text{O}), \text{\AA}$	$h, \text{\AA}$	$R, \text{\AA}$
Experimental [67]			8.93	8.62	4.37	121.5
$G_2\text{-Al}$			9.15	8.74	3.17	67.6
$G_2\text{-Fe}^{3+}$	P1	high spin	9.13	9.01	3.17	238.0
$G_2\text{-Fe}^{2+}$	P1	high spin	9.11	9.08	3.16	284.7

## Intercalation of kaolinite

A 4-step (cascade) intercalation and exfoliation procedure was applied to modify the surface properties of the samples and induce exfoliation of the TO layers via the weakening of the hydrogen bonds as reported in our previous study [28]. Both untreated and acid-washed (11 M HCl, 6 h) Kao samples were subjected to intercalation.

The first step was achieved by mixing 1 g Kao with potassium acetate in a ratio of 70:30, exposing it to laboratory air for 3 days, and drying at 110 °C. The ground, dried precursor (1 g) was then mixed with 7 mL anhydrous ethylene glycol (EG), stirred for 3 h at 150 °C followed by centrifugation (5000 rpm, 5 min), drying, and grinding. This process was repeated once more. The Kao-EG intercalation complex (1 g) was then mixed with 5 mL dry *n*-hexylamine, sealed under Ar atmosphere in a closed vessel, and stirred at ambient temperature for 3 days. Afterward, the sample was separated by centrifugation (5000 rpm, 5 min). This process was repeated 3 times for Kao and 4 times for 11 M-Kao. In the last step, toluene was applied as an exfoliation agent: 5 mL toluene was mixed with 1 g Kao-HA complex and stirred for 5 h. After centrifuge separation, the sample was dried at room temperature, then ground. The majority of surface adsorbed reagents were removed by 2-propanol, acetone, and MilliQ water washing. An additional, oxidative surface treatment was applied to remove minor traces of strongly adsorbed organics by adding 10 mL 10% H<sub>2</sub>O<sub>2</sub> to 1 g of exfoliated Kao-MilliQ water suspension and stirring at 60 °C until bubbling and foam formation ceased. The sample was then centrifuged, dried, and ground before further investigations.

The exfoliated, surface-washed samples are designated as follows: nKao and YM-nKao, where Y is the molarity of the applied HCl.

## Structural characterization

### X-ray powder diffraction (XRD)

XRD measurements were carried out using a Philips PW 3710-type instrument (CuK $\alpha$  radiation,  $\lambda = 1.54056 \text{ \AA}$ , 50 kV, 40 mA), in the 4°–15°  $2\theta$  range with a scanning speed of 0.02°/s and 1 s dwell time. The finely powdered samples were loaded into back-packed mounts to minimize preferential particle orientation. Calcined Al<sub>2</sub>O<sub>3</sub> was applied as reference sample for estimating the instrumental broadening for the average crystallite size calculation. Kaolinite and illite were identified by PDF 00–014–0164 and 00–026–0911 references, respectively.

### Fourier-transform infrared (FTIR) spectroscopy

FTIR spectra were recorded on a Bruker Vertex 70 type equipment with a Bruker Diamond ATR compartment with a

resolution of 2 cm<sup>-1</sup> using a DTGS detector. The recorded spectra are the average of 512 individual scans.

### Transmission electron microscopy measurements (TEM)

Transmission electron microscope investigations were carried out using a FEI Talos F200X type electron microscope with a X-FEG electron source, operated at 200 kV accelerator potential, in conventional transmission (TEM) and scanning modes (STEM). SuperX EDX detector was used for the energy-dispersive X-ray mode. Both scanning and conventional TEM images were recorded. The samples were prepared from aqueous dispersion (MilliQ) by laying a droplet onto a lacy carbon-coated copper grid, which was dried at 60 °C prior to measurement.

### X-ray absorption spectroscopy (XAS)

Fe K-edge XAS of clay samples and references were collected at High Energy Accelerator Research Organization (KEK, Tsukuba, Japan) Photon Factory BL 9C and 12C. The energy of Si(111) double crystal monochromator was calibrated using the first resolved peak of first derivative Fe foil (7111.2 eV, 16.1426°). The third higher harmonic component was removed by detuning of monochromator (*ca.* 60%). The clay samples and references were molded into boron nitrite pellets for the measurements. The intensity of incident and transmitted X-ray (I<sub>0</sub>, I<sub>1</sub>) was measured using N<sub>2</sub>/Ar ion chambers in transmission configuration. Background subtraction, normalization, extracting EXAFS oscillations in *k*-space, and Fourier transformation into the *R*-space were performed on the obtained Fe K-edge spectra. Hanning window function was applied to select *k* range (3–10 Å<sup>-1</sup>) for Fourier-transform. The EXAFS of hematite, goethite, and 11 M HCl-treated kaolin was analyzed with the theoretical scattering pathway calculated from the crystal structure of iron oxides [69, 70] and a computational model of Fe-substituted kaolinite from this study as a reference. The theoretical scattering parameters were obtained using FEFF [71]. These data reduction and analysis were performed using Demeter [72].

### Mössbauer spectroscopy

<sup>57</sup>Fe Mössbauer spectroscopy measurements were performed at room temperature and at *T* = 80 K, using conventional Mössbauer spectrometers (WissEl, Starnberg, Germany and Ranger, Austin Science Associates, Elron, USA) operating in constant acceleration mode. <sup>57</sup>Co source in Rh matrix, kept at ambient temperature, provided the  $\gamma$ -rays for the measurements. For 80 K measurements, the samples were kept at low temperature by using a bath type cryostat (SVT-400-MOSS, Janis, Woburn, MA, USA) filled with liquid nitrogen.



The Mössbauer spectra were evaluated by standard computer-based statistical analysis methods that included fitting the experimental data by a sum of Lorentzians using a least-squares minimization procedure with the help of the MossWinn 4.0i program [73]. The isomer shifts are given relative to  $\alpha$ -Fe reference at room temperature.

### Computational chemistry

The initial structures of the computational models were based on the optimized structure of Generation 2 ( $G_2$ ) cluster model from previous studies of kaolinite [52]. Figure S7 shows the applied  $G_2$  model, including the central honeycomb and the substituted three different positions of  $Al^{3+}$  with  $Fe^{3+}/Fe^{2+}$  ions, furthermore the different nomenclature of hydroxide and oxide groups, namely surface hydroxide ( $sOH^-$ ), inner hydroxide ( $iOH^-$ ), and apical oxide.

( $aO^{2-}$ ). The DFT calculations were carried out with the previously systematically tested pure-GGA (PW91 [74, 75]) with a split valence double zeta basis set (SVP [76, 77]), applying Grimme's empirical dispersion correction (D [77, 78]) and polarizable continuum model (PCM [79, 80]) with the default solvent parameters. All calculations were carried out with Gaussian 16 (rev.A.03) software package [81].

### Acknowledgments

Access to powder X-ray diffraction (Department of Materials Engineering) and TEM imaging instrumentation (Nanolab) at the University of Pannonia is gratefully acknowledged. Part of this study was performed under the approval of Photon Factory Program Advisory Committee (Proposal No. 2018G038).

### Author contributions

BZs contributed to investigation, analysis, data curation, writing—original draft, writing—review and editing, visualization, and funding acquisition. KGy contributed to investigation. TY and ZH contributed to investigation, analysis, and writing—original draft. AT contributed to investigation, analysis, and writing—original draft. VV and CP contributed to investigation. EK contributed to investigation and analysis. EH contributed to conceptualization, resources, supervision, project administration, funding acquisition, writing—review, and editing. JK contributed to resources, supervision, funding acquisition, project administration, writing—review, and editing.

### Funding

Open access funding provided by University of Pannonia. The work of B. Zs. was supported by the ÚNKP-21-4 New National Excellence Program of the Ministry for Innovation and Technology from the source of the National Research, Development, and Innovation Fund.

### Data availability

The authors declare that the data supporting the findings of this study are available within the article and its supplementary information files.

### Code availability

N/A.

### Declarations

**Conflict of interest** The authors declare no conflict of interest. The funders had no role in the design of the study; in the collection, analyses, or interpretation of the data; in the writing of the manuscript, or in the decision to publish the results. No human participants and/or animals were involved in this study.

### Open Access

This article is licensed under a Creative Commons Attribution 4.0 International License, which permits use, sharing, adaptation, distribution and reproduction in any medium or format, as long as you give appropriate credit to the original author(s) and the source, provide a link to the Creative Commons licence, and indicate if changes were made. The images or other third party material in this article are included in the article's Creative Commons licence, unless indicated otherwise in a credit line to the material. If material is not included in the article's Creative Commons licence and your intended use is not permitted by statutory regulation or exceeds the permitted use, you will need to obtain permission directly from the copyright holder. To view a copy of this licence, visit <http://creativecommons.org/licenses/by/4.0/>.

### Supplementary Information

The online version contains supplementary material available at <https://doi.org/10.1557/s43578-022-00768-y>.

### References

1. M.F. Brigatti, E. Galan, B.K.G. Theng, Chapter 2 Structures and Mineralogy of Clay Minerals, in *Dev Clay Sci Handbook Caly Science*, vol. 1, ed. by F. Bergaya, G. Lagaly, M. Vayer (Elsevier, Amsterdam, 2006), pp.19–86
2. R.A. Schoonheydt, C.T. Johnston, Surface and Interface Chemistry of Clay Minerals, in *Dev Clay Sci Handb Caly Sci*, ed. by F. Bergaya, G. Lagaly, M. Vayer (Elsevier, Amsterdam, 2006), pp.87–99
3. X. Zhu, Z. Zhu, X. Lei, C. Yan, Defects in structure as the sources of the surface charges of kaolinite. *Appl. Clay Sci.* **124–125**, 127–136 (2016). <https://doi.org/10.1016/j.clay.2016.01.033>

4. J.W. Stucki, Properties and Behaviour of Iron in Clay Minerals, in *Dev Clay Sci Handb Clay Sci*, vol. 5, ed. by F. Bergaya, G. Lagaly (Elsevier, Amsterdam, 2013), pp.559–611
5. H. Guan, Y. Zhao, 9 - Decontamination application of nanoclays, in *Micro Nano Technol.* ed. by G. Cavallaro, R. Fakhruddin, P.B.T. Pasbakhsh (Elsevier, Amsterdam, 2020), pp.203–224
6. S. Sadjadi, Halloysite-based hybrids/composites in catalysis. *Appl. Clay Sci.* **189**, 105537 (2020). <https://doi.org/10.1016/j.clay.2020.105537>
7. S. Sadjadi, Halloysite nanoclay for development of heterogeneous catalysts, in *Clay Nanoparticles Prop Appl.* ed. by G. Cavallaro, R. Fakhruddin, P. Pasbakhsh (Elsevier, Amsterdam, 2020), pp.275–303
8. C. Li, N. Zhu, S. Yang, X. He, S. Zheng, Z. Sun et al., A review of clay based photocatalysts: role of phyllosilicate mineral in interfacial assembly, microstructure control and performance regulation. *Chemosphere* **273**, 129723 (2021). <https://doi.org/10.1016/j.chemosphere.2021.129723>
9. Y. Zou, Y. Hu, Z. Shen, L. Yao, D. Tang, S. Zhang et al., Application of aluminosilicate clay mineral-based composites in photocatalysis. *J. Environ. Sci.* **115**, 190–214 (2022). <https://doi.org/10.1016/j.jes.2021.07.015>
10. P. Szabó, B. Zsirka, D. Fertig, E. Horváth, T. Csizmadia, J. Kristóf, Delaminated kaolinites as potential photocatalysts: tracking degradation of Na-benzenesulfonate test compound adsorbed on the dry surface of kaolinite nanostructures. *Catal Today* (2017). <https://doi.org/10.1016/j.cattod.2017.01.051>
11. Y. Ruan, L. Kong, Y. Zhong, Z. Diao, K. Shih, L. Hou et al., Review on the synthesis and activity of iron-based catalyst in catalytic oxidation of refractory organic pollutants in wastewater. *J Clean Prod* **321**, 128924 (2021). <https://doi.org/10.1016/j.jclepro.2021.128924>
12. M. Menager, M. Sarakha, Simulated solar light phototransformation of organophosphorus azinphos methyl at the surface of clays and goethite. *Environ Sci Technol* **47**, 765–772 (2013). <https://doi.org/10.1021/es301866f>
13. R.S. Jack, G.A. Ayoko, M.O. Adebajo, R.L. Frost, A review of iron species for visible-light photocatalytic water purification. *Environ Sci Pollut Res* **22**, 7439–7449 (2015). <https://doi.org/10.1007/s11356-015-4346-5>
14. L.R. dos Santos, A.J.S. Mascarenhas, L.A. Silva, Preparation and evaluation of composite with a natural red clay and TiO<sub>2</sub> for dye discoloration assisted by visible light. *Appl. Clay Sci.* **135**, 603–610 (2017). <https://doi.org/10.1016/j.clay.2016.11.002>
15. S. Kakuta, T. Okayama, M. Kato, A. Oda, T. Abe, Clarification of photocatalysis induced by iron ion species naturally contained in a clay compound. *Catal. Sci. Technol.* **1**, 1671 (2011). <https://doi.org/10.1039/c1cy00286d>
16. W.B. Jepson, The composition of kaolinite—an electron microscope microprobe study. *Clays Clay Miner.* **23**, 310–317 (1975). <https://doi.org/10.1346/CCMN.1975.0230407>
17. J.W. Stucki, Chapter 8 Properties and behaviour of iron in clay minerals. *Handb. Clay Sci.* (2006). [https://doi.org/10.1016/S1572-4352\(05\)01013-5](https://doi.org/10.1016/S1572-4352(05)01013-5)
18. E. Murad, Mössbauer spectroscopy of clays, soils and their mineral constituents. *Clay Miner.* **45**, 413–430 (2010). <https://doi.org/10.1180/claymin.2010.045.4.413>
19. D. Richard, N.M. Rendtorff, Local environments in iron-bearing clay minerals by DFT approaches: the case of structural Fe in kaolinite. *Appl. Clay Sci.* **213**, 106251 (2021). <https://doi.org/10.1016/j.clay.2021.106251>
20. A.F. Gualtieri, A. Moen, D.G. Nicholson, XANES study of the local environment of iron in natural kaolinites. *Eur. J. Mineral* **12**, 17–23 (2000). <https://doi.org/10.1127/ejm/12/1/0017>
21. A. Manceau, V.A. Drits, B. Lanson, D. Chateigner, J. Wu, D. Huo et al., Oxidation-reduction mechanism of iron in dioctahedral smectites: II. Crystal chemistry of reduced Garfield nontronite. *Am. Mineral* **85**, 153–172 (2000). <https://doi.org/10.2138/am-2000-0115>
22. K.J.D. MacKenzie, A Mossbauer study of the role of iron impurities in the high temperature reactions of kaolinite minerals. *Clay Miner.* **8**, 151–160 (1969). <https://doi.org/10.1180/claymin.1969.008.2.04>
23. S.A. Fysh, Mössbauer effect studies of iron in Kaolin I. Structural iron. *Clays Clay Miner.* **31**, 285–292 (1983). <https://doi.org/10.1346/CCMN.1983.0310406>
24. N. Finck, M.L. Schlegel, A. Bauer, Structural iron in dioctahedral and trioctahedral smectites: a polarized XAS study. *Phys. Chem. Miner.* **42**, 847–859 (2015). <https://doi.org/10.1007/s00269-015-0768-3>
25. J.W. Stucki, Analysis of iron-bearing clay minerals by electron spectroscopy for chemical analysis (ESCA)\*. *Clays Clay Miner.* **24**, 289–292 (1976). <https://doi.org/10.1346/CCMN.1976.0240603>
26. K. Györfi, V. Vágvolgyi, B. Zsirka, E. Horváth, R.K. Szilágyi, K. Baán et al., Kaolins of high iron-content as photocatalysts: challenges of acidic surface modifications and mechanistic insights. *Appl. Clay Sci.* **195**, 105722 (2020). <https://doi.org/10.1016/j.clay.2020.105722>
27. Y. Zuo, J. Hoigné, Photochemical decomposition of oxalic, glyoxalic and pyruvic acid catalysed by iron in atmospheric waters. *Atmos. Environ.* **28**, 1231–1239 (1994). [https://doi.org/10.1016/1352-2310\(94\)90270-4](https://doi.org/10.1016/1352-2310(94)90270-4)
28. B. Zsirka, E. Horváth, É. Makó, R. Kurdi, J. Kristóf, Preparation and characterization of kaolinite nanostructures: reaction pathways, morphology and structural order. *Clay Miner.* **50**, 329–340 (2015). <https://doi.org/10.1180/claymin.2015.050.3.06>
29. B. Zsirka, E. Horváth, P. Szabó, T. Juzsakova, R.K. Szilágyi, D. Fertig et al., Thin-walled nanoscrolls by multi-step intercalation from tubular halloysite-10 Å and its rearrangement upon peroxide treatment. *Appl. Surf. Sci.* **399**, 245–254 (2017). <https://doi.org/10.1016/j.apsusc.2016.12.053>

30. K. Wada, Lattice expansion of kaolin minerals by treatment with potassium acetate. *Am. Mineral* **46**, 78–91 (1961)
31. A. Weiss, Eine SchichtenschluXverbindung von Kaolinit mit Harnstoff. *Angew. Chem.* **73**, 736–737 (1961). <https://doi.org/10.1002/ange.19610732205>
32. J.E.F.C. Gardolinski, G. Lagaly, Grafted organic derivatives of kaolinite: I. Synthesis, chemical and rheological characterization. *Clay Miner.* **40**, 537–546 (2005). <https://doi.org/10.1180/0009855054040190>
33. B. Singh, Why does halloysite roll? - A new model. *Clays Clay Miner.* **44**, 191–196 (1996)
34. J.E.F.C. Gardolinski, G. Lagaly, Grafted organic derivatives of kaolinite: II. Intercalation of primary n-alkylamines and delamination. *Clay Miner.* **40**, 547–556 (2005). <https://doi.org/10.1180/0009855054040191>
35. É. Makó, I. Dódon, P. Pekker, M. Pósfai, A. Kovács, Z. Ható et al., Nanoscale structural and morphological features of kaolinite nanoscrolls. *Appl. Clay Sci.* **198**, 105800 (2020). <https://doi.org/10.1016/j.clay.2020.105800>
36. H. Cheng, Y. Zhou, Q. Liu, Kaolinite Nanomaterials: Preparation, Properties and Functional Applications, in *Nanomaterials from Clay Minerals*. ed. by W. Wang (Elsevier, Amsterdam, 2019), pp.285–334
37. B. Zhao, L. Liu, H. Cheng, Rational design of kaolinite-based photocatalytic materials for environment decontamination. *Appl. Clay Sci.* **208**, 106098 (2021). <https://doi.org/10.1016/j.clay.2021.106098>
38. A. Shawky, S.M. El-Sheikh, M.N. Rashed, S.M. Abdo, T.I. El-Dosoqy, Exfoliated kaolinite nanolayers as an alternative photocatalyst with superb activity. *J. Environ. Chem. Eng.* **7**, 103174 (2019). <https://doi.org/10.1016/j.jece.2019.103174>
39. M.R. Abukhadra, A.S. Mohamed, A.M. El-Sherbeen, A.T.A. Soliman, Enhanced adsorption of toxic and biologically active levofloxacin residuals from wastewater using clay nanotubes as a novel fixed bed: column performance and optimization. *ACS Omega* **5**, 26195–26205 (2020). <https://doi.org/10.1021/acsomega.0c03785>
40. A. Wiewióra, G.W. Brindley, Potassium acetate intercalation in kaolinite and its removal: effect of material characteristics. *Proc. Int. Clay Conf. Tokyo* **1**, 723–733 (1969)
41. É. Makó, A. Kovács, V. Antal, T. Kristóf, One-pot exfoliation of kaolinite by solvothermal cointercalation. *Appl. Clay Sci.* **146**, 131–139 (2017). <https://doi.org/10.1016/j.clay.2017.05.042>
42. H. Cheng, S. Zhang, Q. Liu, X. Li, R.L. Frost, The molecular structure of kaolinite–potassium acetate intercalation complexes: a combined experimental and molecular dynamic simulation study. *Appl. Clay Sci.* **116–117**, 273–280 (2015). <https://doi.org/10.1016/j.clay.2015.04.008>
43. É. Makó, G. Rutkai, T. Kristóf, Simulation-assisted evidence for the existence of two stable kaolinite/potassium acetate intercalate complexes. *J. Colloid Interface Sci.* **349**, 442–445 (2010). <https://doi.org/10.1016/j.jcis.2010.05.021>
44. J.J. Tunney, Preparation and characterization of two distinct ethylene glycol derivatives of kaolinite. *Clays Clay Miner.* **42**, 552–560 (1994). <https://doi.org/10.1346/CCMN.1994.0420506>
45. M. Janek, K. Emmerich, S. Heissler, R. Nüesch, Thermally induced grafting reactions of ethylene glycol and glycerol intercalates of kaolinite. *Chem. Mater.* **19**, 684–693 (2007). <https://doi.org/10.1021/cm061481+>
46. J. Matusik, E. Wisła-Walsh, A. Gawel, E. Bielańska, K. Bahranowski, Surface area and porosity of nanotubes obtained from kaolin minerals of different structural order. *Clays Clay Miner.* **59**, 116–135 (2011). <https://doi.org/10.1346/CCMN.2011.0590202>
47. J.J. Tunney, C. Detellier, Preparation and characterization of an 84 Å hydrate of kaolinite. *Clays Clay Miner.* **42**, 473–476 (1994). <https://doi.org/10.1346/CCMN.1994.0420414>
48. J. Matusik, A. Gawel, E. Bielańska, W. Osuch, K. Bahranowski, The effect of structural order on nanotubes derived from Kaolin-group minerals. *Clays Clay Miner.* **57**, 452–464 (2009). <https://doi.org/10.1346/CCMN.2009.0570406>
49. A.L. Patterson, The Scherrer formula for X-ray particle size determination. *Phys. Rev.* **56**, 978–982 (1939). <https://doi.org/10.1103/PhysRev.56.978>
50. V.C. Farmer, J.D. Russell, The infra-red spectra of layer silicates. *Spectrochim. Acta* **20**, 1149–1173 (1964). [https://doi.org/10.1016/0371-1951\(64\)80165-X](https://doi.org/10.1016/0371-1951(64)80165-X)
51. V.C. Farmer, Transverse and longitudinal crystal modes associated with OH stretching vibrations in single crystals of kaolinite and dickite. *Spectrochim. Acta Part A* **56**, 927–930 (2000). [https://doi.org/10.1016/S1386-1425\(99\)00182-1](https://doi.org/10.1016/S1386-1425(99)00182-1)
52. A. Táborosi, R.K. Szilágyi, B. Zsirka, O. Fónagy, E. Horváth, J. Kristóf, Molecular treatment of nano-kaolinite generations. *Inorg. Chem.* **57**, 7151–7167 (2018). <https://doi.org/10.1021/acs.inorgchem.8b00877>
53. I.I. Iriarte, S. Petit, F.J. Huertas, S. Fiore, O.O. Grauby, A. Decarreau et al., Synthesis of kaolinite with a high level of Fe<sup>3+</sup> for Al substitution. *Clay Clay Miner.* **53**, 1–10 (2005). <https://doi.org/10.1346/CCMN.2005.0530101>
54. B.-L. Zhu, C.-L. Qi, Y.-H. Zhang, T. Bisson, Z. Xu, Y.-J. Fan et al., Synthesis, characterization and acid-base properties of kaolinite and metal (Fe, Mn, Co) doped kaolinite. *Appl. Clay Sci.* **179**, 105138 (2019). <https://doi.org/10.1016/j.clay.2019.105138>
55. E. Horváth, J. Kristóf, R.L. Frost, Vibrational spectroscopy of intercalated kaolinites. Part I. *Appl. Spectrosc. Rev.* **45**, 130–147 (2010). <https://doi.org/10.1080/05704920903435862>
56. R.L. Frost, J. Kristóf, Raman and Infrared Spectroscopic Studies of Kaolinite Surfaces Modified by Intercalation, in *Interface Sci. Technol. Clay Surfaces: Fundam. Appl.*, 1st edn., ed. by F. Wypych, K.G. Satyanarayana (Elsevier, Brisbane, 2004), pp.184–215
57. R.L. Ledoux, J.L. White, Infrared studies of hydrogen bonding interaction between kaolinite surfaces and intercalated

- potassium acetate, hydrazine, formamide, and urea. *J. Colloid Interface Sci.* **21**, 127–152 (1966). [https://doi.org/10.1016/0095-8522\(66\)90029-8](https://doi.org/10.1016/0095-8522(66)90029-8)
58. H. Cheng, J. Yang, R.L. Frost, Q. Liu, Z. Zhang, Thermal analysis and Infrared emission spectroscopic study of kaolinite-potassium acetate intercalate complex. *J. Therm. Anal. Calorim.* **103**, 507–513 (2011). <https://doi.org/10.1007/s10973-010-0917-3>
  59. Q. Liu, X. Li, H. Cheng, Insight into the self-adaptive deformation of kaolinite layers into nanoscrolls. *Appl. Clay Sci.* **124–125**, 175–182 (2016). <https://doi.org/10.1016/j.clay.2016.02.015>
  60. E. Murad, J. Cashion, *Mössbauer Spectroscopy of Environmental Materials and Their Industrial Utilization* (Springer, US, Boston, MA, 2004)
  61. J.W. Stucki, B.A. Goodman, U. Schwertmann, *Iron in Soils and Clay Minerals*, vol. 902 (Springer, Dordrecht, 1987)
  62. J.M.D. Coey, *Magnetic Properties of Iron in Soil Iron Oxides and Clay Minerals. Iron Soils Clay Mineral* (Springer, Dordrecht, 1988), pp.397–466
  63. P.S. Sidhu, Dissolution of iron oxides and oxyhydroxides in hydrochloric and perchloric acids. *Clays Clay Miner.* **29**, 269–276 (1981). <https://doi.org/10.1346/CCMN.1981.0290404>
  64. U. Schwertmann, Solubility and dissolution of iron oxides. *Plant Soil* **130**, 1–25 (1991). <https://doi.org/10.1007/BF00011851>
  65. P. Rengasamy, Isomorphous substitution of iron for aluminium in some soil kaolinites. *Clays Clay Miner.* **23**, 211–214 (1975). <https://doi.org/10.1346/CCMN.1975.0230308>
  66. E. Murad, U. Wagner, The Mössbauer spectrum of illite. *Clay Miner.* **29**, 1–10 (1994). <https://doi.org/10.1180/claymin.1994.029.1.01>
  67. X. Li, Q. Liu, H. Cheng, S. Zhang, R.L. Frost, Mechanism of kaolinite sheets curling via the intercalation and delamination process. *J. Colloid Interface Sci.* **444**, 74–80 (2015). <https://doi.org/10.1016/j.jcis.2014.12.039>
  68. B. Zsirka, V. Vágvölgyi, K. Gyórfi, E. Horváth, R.K. Szilágyi, E. Szabó-Bárdos et al., Compositional, structural, and surface characterization of heat-treated halloysite samples: influence of surface treatment on photochemical activity. *Appl. Clay Sci.* **212**, 106222 (2021). <https://doi.org/10.1016/j.clay.2021.106222>
  69. R.L. Blake, R.E. Hessevick, T. Zoltai, L.W. Finger, Refinement of the hematite structure. *Am. Mineral J. Earth Planet Mater.* **51**, 123–129 (1966)
  70. H. Yang, R. Lu, R.T. Downs, G. Costin, Goethite,  $\alpha$ -FeO(OH), from single-crystal data. *Acta Crystallogr. Sect. E Struct. Rep.* **62**, i250–i252 (2006). <https://doi.org/10.1107/S1600536806047258>
  71. M. Newville, EXAFS analysis using FEFF and FEFFIT. *J. Synchrotron Radiat.* **8**, 96–100 (2001). <https://doi.org/10.1107/S0909049500016290>
  72. B. Ravel, M. Newville, ATHENA, ARTEMIS, HEPHAESTUS: data analysis for X-ray absorption spectroscopy using IFEFFIT. *J. Synchrotron Radiat.* **12**, 537–541 (2005). <https://doi.org/10.1107/S0909049505012719>
  73. Z. Klencsár, E. Kuzmann, A. Vértes, User-friendly software for Mössbauer spectrum analysis. *J. Radioanal Nucl. Chem. Artic.* **210**, 105–118 (1996). <https://doi.org/10.1007/BF02055410>
  74. J.P. Perdew, J.A. Chevary, S.H. Vosko, K.A. Jackson, M.R. Pederson, D.J. Singh et al., Atoms, molecules, solids, and surfaces: applications of the generalized gradient approximation for exchange and correlation. *Phys. Rev. B* **46**, 6671–6687 (1992). <https://doi.org/10.1103/PhysRevB.46.6671>
  75. J.P. Perdew, Y. Wang, Accurate and simple analytic representation of the electron-gas correlation energy. *Phys. Rev. B* **45**, 13244–13249 (1992). <https://doi.org/10.1103/PhysRevB.45.13244>
  76. A. Schäfer, H. Horn, R. Ahlrichs, Fully optimized contracted Gaussian basis sets for atoms Li to Kr. *J. Chem. Phys.* **97**, 2571–2577 (1992). <https://doi.org/10.1063/1.463096>
  77. A. Schäfer, C. Huber, R. Ahlrichs, Fully optimized contracted Gaussian basis sets of triple zeta valence quality for atoms Li to Kr. *J. Chem. Phys.* **100**, 5829–5835 (1994). <https://doi.org/10.1063/1.467146>
  78. S. Grimme, J. Antony, S. Ehrlich, H. Krieg, A consistent and accurate ab initio parametrization of density functional dispersion correction (DFT-D) for the 94 elements H–Pu. *J. Chem. Phys.* **132**, 154104 (2010). <https://doi.org/10.1063/1.3382344>
  79. S. Miertuš, E. Scrocco, J. Tomasi, Electrostatic interaction of a solute with a continuum. A direct utilization of AB initio molecular potentials for the prevision of solvent effects. *Chem. Phys.* **55**, 117–129 (1981). [https://doi.org/10.1016/0301-0104\(81\)85090-2](https://doi.org/10.1016/0301-0104(81)85090-2)
  80. J. Tomasi, B. Mennucci, R. Cammi, Quantum mechanical continuum solvation models. *Chem. Rev.* **105**, 2999–3094 (2005). <https://doi.org/10.1021/cr9904009>
  81. M.J. Frisch, G. W. Trucks, H. B. Schlegel, G. E. Scuseria, M. A. Robb, J. R. Cheeseman, et al. Gaussian 16 (G16\_a03) 2016: Gaussian 16, Revision A.03.

**Publisher's Note** Springer Nature remains neutral with regard to jurisdictional claims in published maps and institutional affiliations.